

Article

Preparation of g-C₃N₄/Bismuth Iodide/Tourmaline Composites and Their Photodegradation Performance of Amaranthine

Junsheng Li ¹, Jiahui Li ¹, Liming Jiang ¹, Meiyang Xu ¹, Zhi Xia ¹, Chong Tan ¹, Yuyang Wang ^{2,*} and Jinlong Zuo ^{1,*}

¹ School of Food Engineering, Harbin University of Commerce, Harbin 150028, China; 101719@hrbcu.edu.cn (J.L.); 101716@hrbcu.edu.cn (L.J.); 101716@hrbcu.edu.cn (L.J.); xu_951204@163.com (M.X.); 102820@hrbcu.edu.cn (Z.X.); 102776@hrbcu.edu.cn (C.T.)

² School of Light Industry, Harbin University of Commerce, Harbin 150028, China

* Correspondence: wangyuyanglover@163.com (Y.W.); 101760@hrbcu.edu.cn (J.Z.)

Abstract: In this study, g-C₃N₄/BiOI/tourmaline composites were synthesized by loading BiOI and tourmaline on g-C₃N₄ nanofilms using g-C₃N₄, BiOI, and tourmaline as raw materials, aiming to optimize the photocatalytic degradation of amaranth red dye wastewater (AR). Single-factor experiments were conducted to optimize the degradation process. The findings indicate that a degradation rate of 95.88% can be achieved for AR within 150 min of light exposure, given a g-C₃N₄/BiOI/tourmaline dosage of 1 g/L, an initial pH level of 3 for the AR, and an initial AR concentration of 10 mg/L. Upon repeating the experiment for five cycles, the composite exhibited 83.10% activity, demonstrating its stability. Various analytical techniques were employed for material characterization: X-ray diffraction (XRD) to ascertain the crystalline structure, field-emission scanning electron microscopy (FESEM) to evaluate morphology, X-ray photoelectron spectroscopy (XPS) for elemental analysis, ultraviolet–visible diffuse reflectance spectroscopy (UV-vis DRS) for optical properties, and photoluminescence (PL) spectroscopy to analyze the recombination of excited electrons and holes. Free radical masking experiments further elucidated the photocatalytic mechanism, revealing that the primary active species in the degradation process is the superoxide anion (O₂^{•−}). This research offers a novel approach to address the limitations of n-type metal-free semiconductor photocatalysts.

Keywords: carbon nitride film; dot bismuth oxide; tourmaline; photocatalysis; food dye wastewater; amaranthine red



Citation: Li, J.; Li, J.; Jiang, L.; Xu, M.; Xia, Z.; Tan, C.; Wang, Y.; Zuo, J. Preparation of g-C₃N₄/Bismuth Iodide/Tourmaline Composites and Their Photodegradation Performance of Amaranthine. *Coatings* **2023**, *13*, 1983. <https://doi.org/10.3390/coatings13121983>

Academic Editor: Alexandru Enesca

Received: 16 October 2023

Revised: 17 November 2023

Accepted: 20 November 2023

Published: 22 November 2023



Copyright: © 2023 by the authors. Licensee MDPI, Basel, Switzerland. This article is an open access article distributed under the terms and conditions of the Creative Commons Attribution (CC BY) license (<https://creativecommons.org/licenses/by/4.0/>).

1. Introduction

Food dyes are prevalent in the food industry and find applications in a diverse range of food products [1]. Wastewater generated from these processes is typically characterized by high volume, complex chemical makeup, and elevated chromaticity. These characteristics can result in unpleasant odors and turbidity, deteriorate water quality, and even lead to mortality among aquatic organisms, thereby contributing to severe water pollution [2]. Current industrial approaches to mitigating this issue predominantly include physical adsorption and microbial treatment techniques. Physical adsorption, however, suffers from drawbacks such as low efficiency and high operational costs, and may necessitate further treatment to avoid secondary pollution [3]. On the other hand, microbial treatment methods have strict requirements concerning pH, nutrient composition, and temperature. These constraints make it challenging to apply microbial treatments to wastewater with a complex chemical profile. Furthermore, the need for large treatment areas and extended processing times limits their practical applicability [4].

As a recognized “green technology”, photocatalytic degradation treatment has the advantages of non-toxicity, high efficiency, and low cost, and can be used to treat wastewater containing food dyes [5]. g-C₃N₄ has received much attention as a common photocatalyst because of its easy preparation, cost-effectiveness, and narrow band gap. However, due to some important limitations, in order to overcome the disadvantages of some photocatalysts

such as smaller specific surface area, poor light absorption, short quantum efficiency, and higher recombination rate of induced electron–hole pairs, researchers have combined them with BiOI by constructing heterojunction structures such as homo-type, conventional type II and Z, and p-n type. The e^- and h^+ can be separated effectively, thus improving the activity of the composite catalysts [6]. Sun et al. [7] prepared graphite-phase carbon nitride nanofilms ($g-C_3N_4$) through thermal polymerization using melamine as a precursor and synthesized bismuth iodide (BiOI) in situ on its surface to construct graphite-phase carbon nitride–bismuth iodide composites. The results showed that the maximum performance of the BiOI/ $g-C_3N_4$ catalyst for the adsorption and degradation of methyl orange was achieved when the amount ratio of BiOI to $g-C_3N_4$ was 0.5, and 52% of methyl orange was adsorbed for 60 min and 98% of methyl orange was degraded through photocatalysis for 120 min.

Tourmaline has permanent spontaneous polarization, thermoelectricity, infrared radiation, and good adsorption properties, which contribute to the adsorption of organic matter or promote the formation of hydroxyl radicals and reduce the high electron–hole recombination rate, making it an environmentally friendly material [8]. However, the preparation of $g-C_3N_4$ /BiOI containing tourmaline has rarely been reported so far. Therefore, in this study, a new photocatalyst $g-C_3N_4$ /BiOI/tourmaline was synthesized. The photocatalytic performance was investigated by measuring the degradation of AR under light illumination, and a high removal efficiency was obtained.

2. Experiment

2.1. Experimental Reagents

Melamine ($C_3H_6N_6$), analytically pure, molecular weight 126.12, purchased from Tianjin Guang Fu Fine Chemical Research Institute (Tianjin, China); anhydrous ethanol (C_2H_5OH), analytically pure, molecular weight 46.07, purchased from Tianjin Fuyu Fine Chemical Co. (Tianjin, China); bismuth nitrate ($Bi(NO_3)_3 \cdot 5H_2O$), analytically pure, molecular weight 485.07, purchased from Tianjin Tian Li Chemical Reagent Co. (Tianjin, China); potassium iodide (KI), analytically pure, molecular weight 166.00, purchased from Tianjin Xin Tai Yi Technology Co. (Tianjin, China); polyvinylpyrrolidone (PVP), analytically pure, average molecular weight 1,300,000, purchased from Tianjin Guang Fu Fine Chemical Research Institute (Tianjin, China); ethylene glycol ($HOCH_2CH_2OH$), analytically pure, molecular weight 62.068, purchased from Tianjin Fuyu Fine Chemical Co. (Tianjin, China); Amaranth Red (AR), analytically pure, molecular weight 604.473, purchased from Nanjing Chemical Reagent Co., Ltd. (Nanjing, China); tourmaline, 10,000 mesh, molecular weight 64.099, purchased from Ling shou County Jingwei Mineral Products Processing Plant (Hebei, China).

2.2. Synthesis of $g-C_3N_4$ /BiOI/Tourmaline

Preparation of $g-C_3N_4$ nanofilm: $g-C_3N_4$ was synthesized using thermal polycondensation method. An amount of 5 g of melamine was put into a crucible with a lid and calcined in a muffle furnace at a temperature of 600 °C for 4 h with a heating rate of 5 °C/min and then washed with anhydrous ethanol and deionized water alternately; the crude samples were taken out of the apparatus at the end of the process and then ground and dried in an agate mortar. After washing with anhydrous ethanol and deionized water alternately and drying, a yellowish powder of $g-C_3N_4$ was obtained. The powder was then pressed into thin sheets to form a film.

Preparation of BiOI: Solution “A” was synthesized by dissolving 1.9403 g of bismuth nitrate ($Bi(NO_3)_3 \cdot 5H_2O$) and 0.1 g of polyvinylpyrrolidone (PVP) in 38 mL of water. In addition, a solution called “B” was prepared by dissolving 0.6640 g of potassium iodide (KI) in 38 mL of ethylene glycol. Solution A was slowly added to solution B under magnetic stirring, and then continuously stirred for a period of time and transferred to a 100 mL high-pressure-reactor Teflon-lined steel autoclave. The hydrothermal reaction was carried out at 180 °C for 16 h and then naturally cooled to room temperature, washed three times

using deionized water and anhydrous ethanol in turn, and dried in an oven at 80 °C. After naturally cooling to room temperature, the reddish brown BiOI sample was obtained through grinding.

Preparation of g-C₃N₄/BiOI: The g-C₃N₄/BiOI photocatalyst was prepared through ultrasonic stirring. The g-C₃N₄ and BiOI powders were first co-dispersed in 100 mL of aqueous ethanol solution. The mixture was ultrasonicated at room temperature for 30 min, followed by magnetic stirring for 24 h. And the mixture was dried at 80 °C. The powder was then pressed into a thin sheet using a press. The g-C₃N₄/BiOI photocatalyst was obtained.

Preparation of g-C₃N₄/BiOI/tourmaline: The synthesized g-C₃N₄/BiOI material was mixed with a 1.0% mass ratio of tourmaline through the above method. The mixture was dried and the powder was pressed into thin sheets using a press. The final g-C₃N₄/BiOI/tourmaline catalyst was obtained.

2.3. Photocatalytic Activity Test

The absorbance of 10 mg/L of AR solution was measured in the range of 350–650 nm, and the wavelength corresponding to its maximum absorbance was found to determine the maximum absorption wavelength of AR solution. The standard curve of wavelength (λ)–absorbance (A) is plotted in Figure 1.

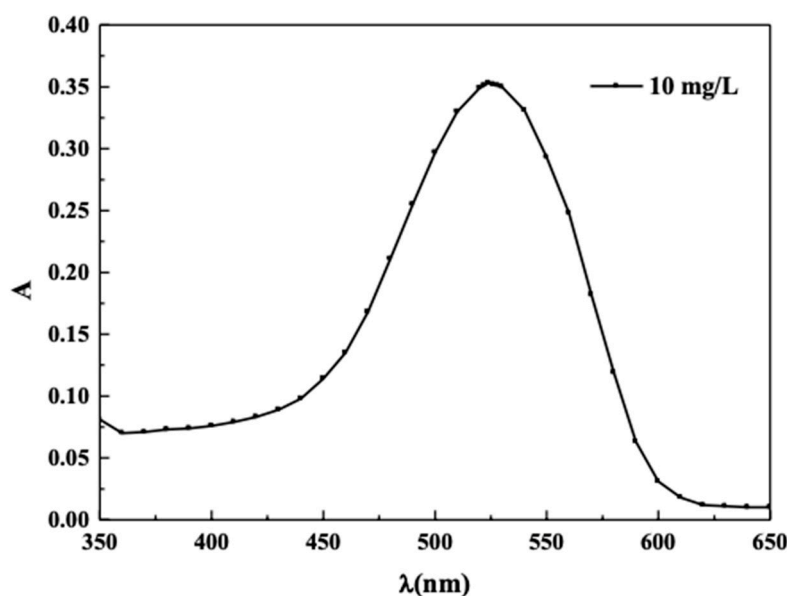


Figure 1. Absorbance spectrum of an AR solution at 10 mg/L.

From Figure 1, it can be seen that the maximum absorption wavelength of the AR solution is located at 522 nm, so the absorbance of the AR solution in the subsequent degradation experiments was measured at the wavelength of 522 nm. A series of AR solutions of 1 mg/L, 2 mg/L, 3 mg/L, 4 mg/L, 5 mg/L, 6 mg/L, 7 mg/L, 8 mg/L, 9 mg/L, and 10 mg/L were prepared, and the absorbance values were measured at 522 nm. The concentration (C)–absorbance (A) standard curves are plotted in Figure 2.

As can be seen from Figure 2, the concentration of AR solution shows a good linear relationship with the area under the absorbance curve of $R^2 = 0.9997$, so it can be assumed that the degradation rate of AR solution can be calculated by Equation (1):

$$\eta = [(C_0 - C)/C_0] \times 100\% = [(A_0 - A)/A_0] \times 100\% \quad (1)$$

where C_0 is the initial concentration of the AR solution; C is the concentration of the AR solution at the time of reaction, and A_0 is the corresponding absorbance values.

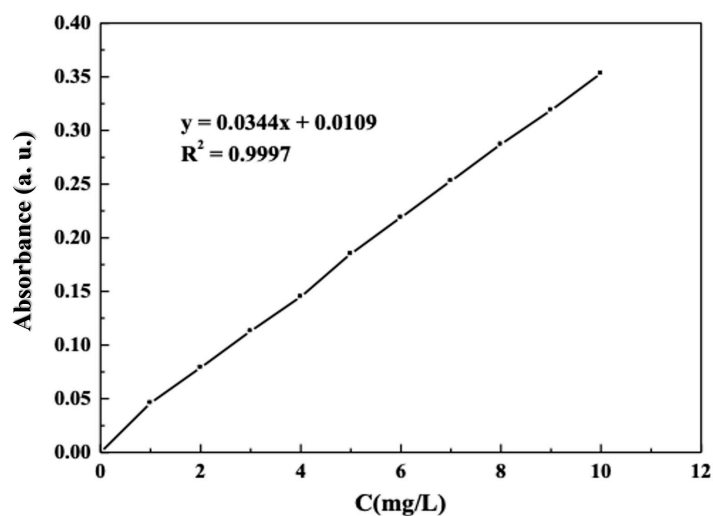
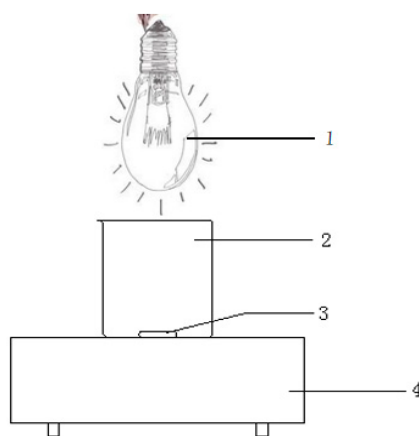


Figure 2. Standard curve of AR solution.

The photocatalytic activity of the prepared C_3N_4 /BiOI/tourmaline catalysts was evaluated using a self-designed reactor (100 mL quartz beaker) under visible-light irradiation from a 250 W mercury lamp (Shanghai Yamin Lighting Co., Shanghai, China) at a distance of 10 cm from the quartz beaker. Before irradiation, 10 mg of C_3N_4 /BiOI/tourmaline catalyst was dispersed in 10 mg/L AR solution and stirred vigorously and thoroughly in the dark for 30 min to establish the adsorption–desorption equilibrium between the photocatalyst surface and the contaminant molecules. The amaranthine degradation efficiency was determined by applying a UV-2550 spectrophotometer (Shanghai Yuan analytical Instrument Co., Shanghai, China) with a wavelength of 522 nm and taking samples at ten-minute intervals. The 100 catalysts that had undergone one degradation were recovered, dried, and then subjected to the same photocatalytic degradation experiment, which was repeated four times to determine the stability of the C_3N_4 /BiOI/tourmaline catalysts. To investigate the photocatalytic mechanism, disodium ethylenediaminetetraacetate (Na_2 -EDTA) as a trapping agent for h^+ group, p-benzoquinone (BQ) as a trapping agent for $-O_2^-$ group, and isopropyl alcohol (IPA) as a trapping agent for $-OH$ group were added to the reaction system and free radical scavenging experiments were performed to determine the main active substances in the photocatalytic process. A diagram of the photodegradation setup for the photocatalytic experiment is shown in Figure 3.



1—Mercury lamp; 2—Quartz beaker; 3—Rotor; 4—Magnetic stirrer

Figure 3. The schematic diagram of photocatalytic degradation.

2.4. Sample Characterization

The crystalline phase structure of the samples was determined using a D8-ADVANCE X-ray diffractometer (XRD) (Bruker, Mannheim, Germany) in the 2θ range ($10\text{--}80^\circ$) with Cu-K α radiation ($\lambda = 1.54056 \text{ \AA}$). The morphology of the products was performed using a Hitachi S-4800 field emission scanning electron microscope (FESEM) (Hitachi, Tokyo, Japan). X-ray photoelectron spectroscopy (XPS) was performed on an ESCALAB 250 instrument (thermo Fisher Scientific, Waltham, MA, USA) with Al K α radiation ($h\nu = 1486.6 \text{ eV}$). The UV-vis diffuse reflectance spectra (UV-vis DRS) of the synthesized photocatalysts were recorded using a Shimadzu UV-2550 spectrometer. (Shanghai Yuan analytical Instrument Co., Shanghai, China) Fourier transform infrared spectroscopy (FT-IR) analysis was applied to study the chemical bonding and functional group composition of the products using a VERTEX 80 FT-IR spectrometer (Bruker, Mannheim, Germany) with a spectral range of $4000\text{--}400 \text{ cm}^{-1}$ and a resolution of 0.07 cm^{-1} . Photoluminescence (PL) spectra were measured on a Hitachi F-7000 fluorescence spectrophotometer ($\lambda_{\text{ex}} = 325 \text{ nm}$).

3. Results and Discussion

3.1. Sample Characterization and Analysis

The material composition of the photocatalytic materials was characterized using XRD. The XRD diffraction spectra for each sample are presented in Figure 4. The spectra reveal that in the g-C₃N₄/BiOI/tourmaline composites, distinct diffraction peaks at 2θ values of 11.4° , 13.1° , and 32.2° correspond to tourmaline. These peaks appear in addition to those of g-C₃N₄ and BiOI. Notably, diffraction peaks typically associated with tourmaline at 2θ values of 22.4° , 26.6° , 30.3° , and 34.9° were faint or absent. This absence is likely due to the overlap of BiOI peaks with those of tourmaline and the low content of tourmaline in the sample [9].

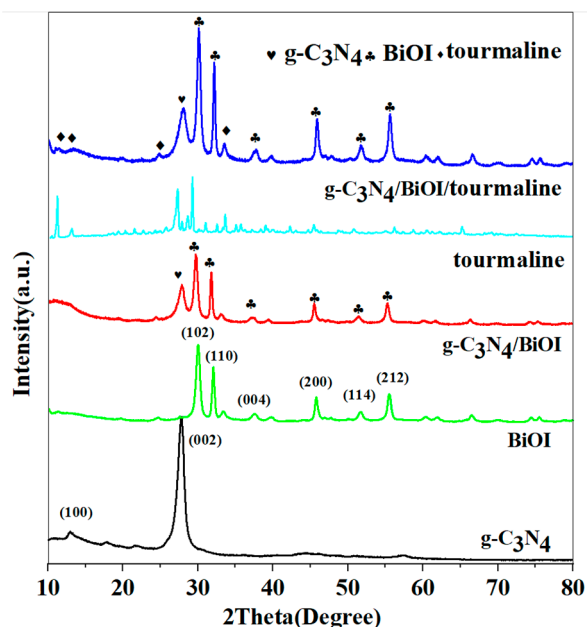


Figure 4. XRD spectrum of g-C₃N₄, BiOI, g-C₃N₄/BiOI, tourmaline, and g-C₃N₄/BiOI/tourmalines.

The SEM images of g-C₃N₄, tourmaline, and g-C₃N₄/BiOI/tourmaline composites are shown in Figure 5. From the laminar structure of g-C₃N₄ stacking seen in Figure 5a, the original natural mineral tourmaline in Figure 5b, the fine particles that can be clearly seen, BiOI in Figure 5c, and the g-C₃N₄/BiOI/tourmaline composite in Figure 5d, it can be observed that there are many small particles on the surface of the laminar g-C₃N₄ and BiOI (red part in the figure), which have the same morphology as tourmaline. It is confirmed that the tourmaline gas was successfully incorporated into g-C₃N₄/BiOI.

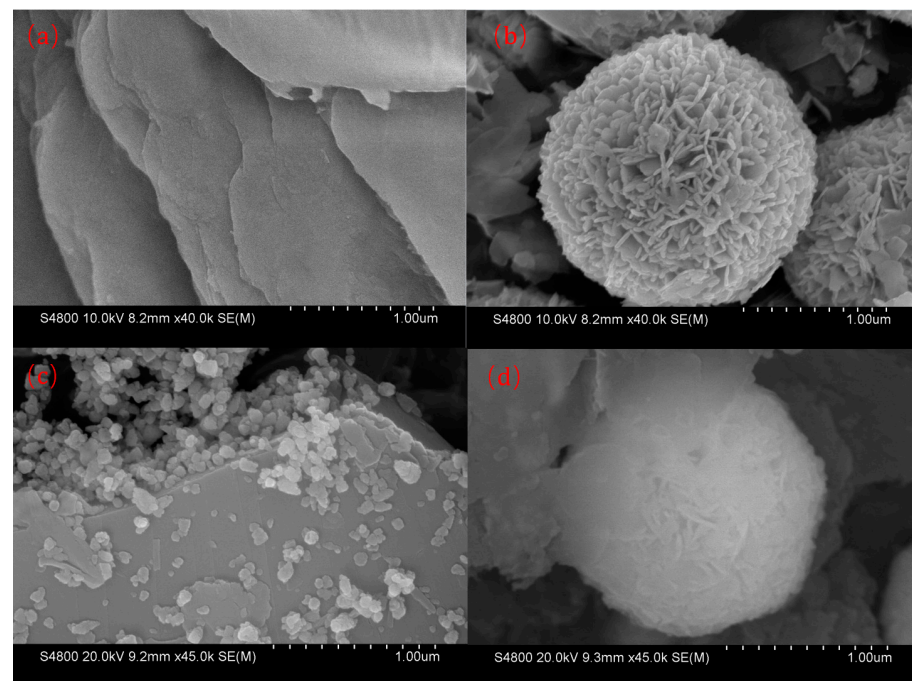


Figure 5. SEM images of g-C₃N₄ (a), BiOI (b), tourmaline (c), and g-C₃N₄/BiOI/tourmaline (d).

The elemental valence and chemical composition of g-C₃N₄, g-C₃N₄/BiOI, and g-C₃N₄/BiOI/tourmaline were analyzed using XPS, and the results are shown in Figure 6. Figure 6a shows the full spectra of the samples, and elemental C, N, and O are observed in the measured spectra from 0 to 1200 eV for both the g-C₃N₄ material and the g-C₃N₄/BiOI composite; elemental Bi and I are also present in the g-C₃N₄/BiOI composite, whereas the characteristic peaks of the elemental Mg and Si are also observed in g-C₃N₄/BiOI/tourmaline, from the tourmaline. Therefore, the results of XPS tests indicate that the g-C₃N₄/BiOI composites and g-C₃N₄/BiOI/tourmaline composites were successfully prepared and do not contain other impurity elements. Figure 6b shows the XPS high-resolution spectra of the C 1s state. The peak at 284.7 eV for pure g-C₃N₄ corresponds to C–C or C=C, the peak at 287.6 eV is related to the sp² hybridization of g-C₃N₄ (N–C=N) [10], and the peaks at 284.7 eV and 288.1 eV appearing in the C 1s spectra of g-C₃N₄/BiOI and the two peaks at 288.1 eV and 284.6 eV in g-C₃N₄/BiOI/tourmaline are the same as the two peaks in pure g-C₃N₄. Figure 6c shows the XPS high-resolution spectra of the N 1s state. The N 1s spectra of pure g-C₃N₄ and g-C₃N₄/BiOI are basically the same, and the main peaks at 398.8 eV and 398.3 eV can be attributed to the presence of nitrogen sp² hybridized by the bonding of the N of g-C₃N₄ with the C in the g-C₃N₄ and g-C₃N₄/BiOI composites. And the peak observed at 400.2 eV is assigned to the tertiary nitrogen group, which is in good agreement with previous reports [11]. The N 1s spectra of g-C₃N₄/BiOI/tourmaline are essentially the same as the other two samples, with peaks observed at 398.7 eV and 400.4 eV. As shown in Figure 6d, showing the XPS Gaussian fitting curve of the O 1s state, two different types of O are present in the g-C₃N₄/BiOI sample: the lower binding energy at 530.8 eV represents the hydroxyl (–OH) adsorbed on the lattice oxygen of BiOI, whereas the higher binding energy at 532.2 eV correlates with chemisorbed oxygen in the oxygen-deficient region of the surface (surface oxygen and hydroxyl) [12]. And surface oxygen and hydroxyl groups are able to trap photogenerated electrons and holes to generate strongly oxidizing hydroxyl radicals. The comparison with g-C₃N₄/BiOI shows that g-C₃N₄/BiOI/tourmaline has only one oxygen peak with a higher binding energy of 532.5 eV, while it does not have the lattice oxygen of BiOI, which may be due to the fact that the addition of tourmaline improves the surface structure of g-C₃N₄/BiOI, and the electric field of tourmaline causes the decomposition of water to produce more –OH, which leads to an increase in reactive oxygen in water [13]. The peaks located at 164.3 eV

and 158.9 eV shown in Figure 6e correspond to the binding energies of Bi 4f_{5/2} and Bi 4f_{7/2}, respectively, confirming the presence of elemental Bi in the form of Bi³⁺ [14]. The peaks located at 630.1 eV and 618.6 eV shown in Figure 6f correspond to the binding energies of I 3d_{3/2} and I 3d_{5/2}, respectively, confirming the presence of the element I in the I[−] form. The g-C₃N₄/BiOI has peaks in the spectra of the corresponding monomers, and the XPS results are sufficient evidence that the g-C₃N₄/BiOI composite catalysts were successfully synthesized, which is consistent with the previous XRD results. In addition, the small shifts in binding energies indicate a change in their chemical environments, further confirming that the heterojunction between g-C₃N₄ and BiOI was successfully constructed. Figure 6g shows peaks located at 50.1 eV and 48.5 eV, which correspond to the binding energies of Mg 2p_{1/2} and Mg 2p_{3/2}, respectively, and Figure 6h shows peaks located at 101.9 eV, which correspond to the binding energy of Si 2p; in addition, the small shifts in the binding energies suggest a change in their chemical environments.

The optical properties of g-C₃N₄/BiOI/tourmaline materials were investigated using UV-Vis diffuse reflectance spectroscopy, as illustrated in Figure 7a. Band gap values for g-C₃N₄, BiOI, g-C₃N₄/BiOI, and g-C₃N₄/BiOI/tourmaline samples were calculated and are presented in Figure 7b. Comparative analysis of the UV-Vis DRS spectra for g-C₃N₄, BiOI, g-C₃N₄/BiOI, and g-C₃N₄/BiOI/tourmaline was conducted to elucidate the optical characteristics of these samples. According to Figure 7a, the absorption edge for g-C₃N₄/BiOI/tourmaline ranges from approximately 430 nm to 520 nm, showing minimal variation when compared to g-C₃N₄ and g-C₃N₄/BiOI. As depicted in Figure 7b, the band gaps for g-C₃N₄, BiOI, g-C₃N₄/BiOI, and g-C₃N₄/BiOI/tourmaline are 2.73 eV, 1.85, 2.6 eV, and 2.52 eV, respectively. The narrowing of the band gaps is likely attributable to the co-doping of BiOI and tourmaline, which alters the original coordination field of g-C₃N₄. This alteration likely enhances the Stark effect, thereby improving light absorption efficiency [15].

The optical properties and excited electron and hole complexes of g-C₃N₄, g-C₃N₄/BiOI, and g-C₃N₄/BiOI/tourmaline materials were analyzed through photoluminescence (PL) spectroscopy. The obtained PL spectral results are shown in Figure 8. As can be seen from the figures, the PL spectra of g-C₃N₄, g-C₃N₄/BiOI and g-C₃N₄/BiOI/tourmaline exhibit a wide emission range from 400 to 600 nm, with the peak near 475 nm. The visible emission peak can be attributed to the defect-induced correlated emission, the addition of tourmaline resulted in a substantial decrease in fluorescence intensity compared to g-C₃N₄ and g-C₃N₄/BiOI, and the decrease in fluorescence intensity could be attributed to the inhibitory effect on the electron–hole complex due to the polarized electric field of tourmaline, proving that the relatively long lifetime of the carrier charge in the composites is more likely to be involved in the photocatalytic process, resulting in better degradation efficiency [16].

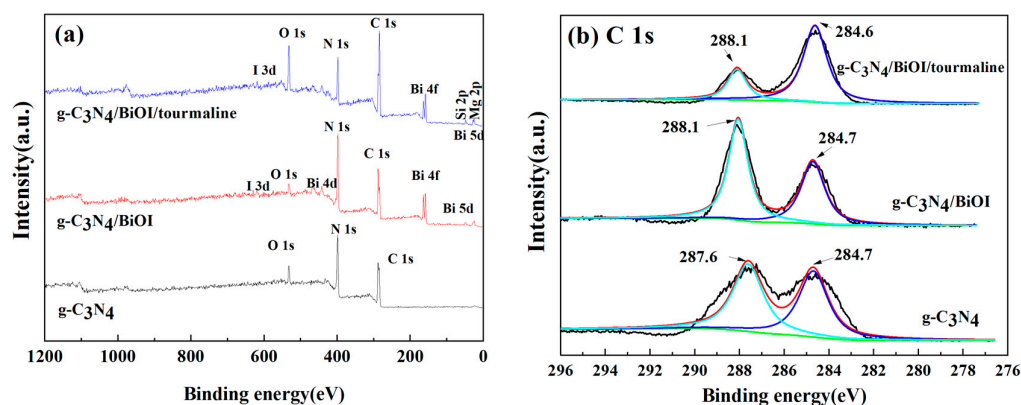


Figure 6. Cont.

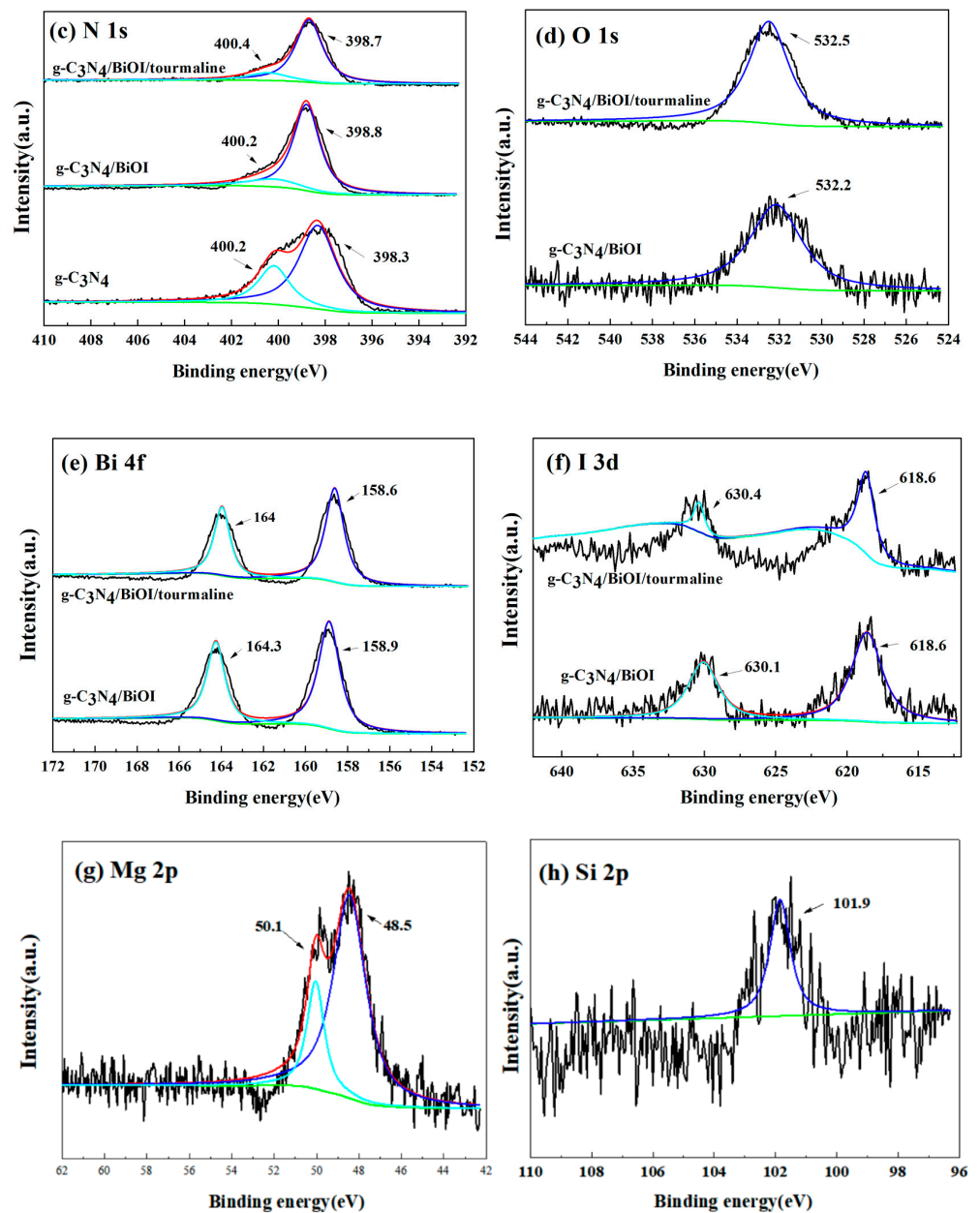


Figure 6. High-resolution XPS spectra of g-C₃N₄/BiOI/tourmaline: (a) all spectra; (b) C 1s; (c) N 1s; (d) O 1s; (e) Bi 4f; (f) I 3d; (g) Mg 2p; (h) Si 2p.

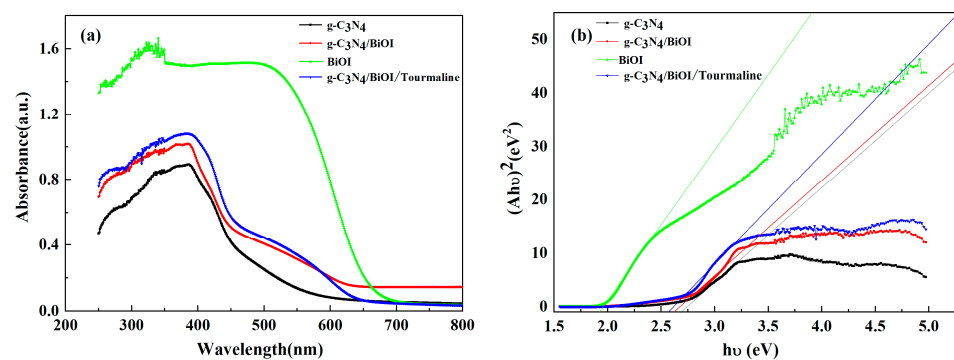


Figure 7. (a) UV-Vis DRS spectra of g-C₃N₄, BiOI, g-C₃N₄/BiOI, and g-C₃N₄/BiOI/tourmaline; (b) estimated band gap.

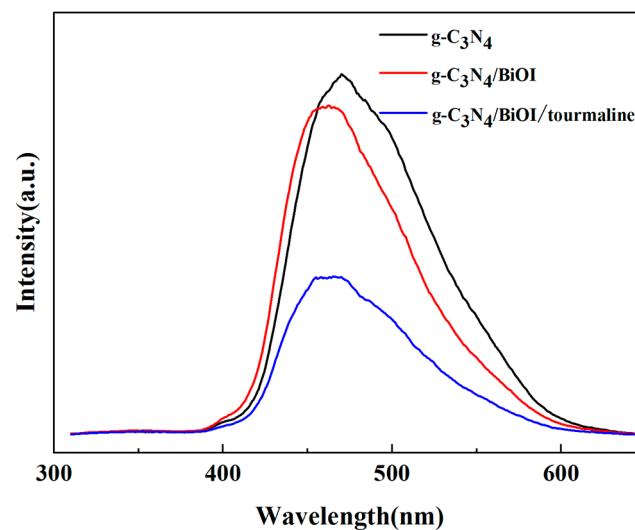


Figure 8. PL spectra of $g\text{-C}_3\text{N}_4$, $g\text{-C}_3\text{N}_4/\text{BiOI}$, and $g\text{-C}_3\text{N}_4/\text{BiOI}/\text{tourmaline}$.

3.2. Photocatalytic Performance Testing

In order to investigate the photocatalytic performance of $g\text{-C}_3\text{N}_4/\text{BiOI}/\text{tourmaline}$ composites under light irradiation, degradation experiments were conducted on AR solutions. The degradation experiments of the AR solution with different combinations of materials were compared, and the experimental results are shown in Figure 9. As shown in Figure 9a, the efficiencies of $g\text{-C}_3\text{N}_4$ and $g\text{-C}_3\text{N}_4/\text{BiOI}$ were 44.21% and 69.48%, respectively. This is due to the fact that the addition of BiOI expands the visible-light response range of $g\text{-C}_3\text{N}_4$, forms heterojunctions in the composites, and improves the photocatalytic efficiency. The degradation rate of tourmaline was 7.56% and did not have a catalytic effect by itself, while both $g\text{-C}_3\text{N}_4/\text{tourmaline}$ and $\text{BiOI}/\text{tourmaline}$ showed improved degradation compared to pure $g\text{-C}_3\text{N}_4$ and BiOI, 54.87% and 65.65%, respectively, and the addition of tourmaline improved the efficiency of a single material. $g\text{-C}_3\text{N}_4/\text{BiOI}/\text{tourmaline}$ catalysts showed higher removal rates than any of the other catalysts, and the degradation rate was 84.43% after 150 min of light. $g\text{-C}_3\text{N}_4/\text{BiOI}/\text{tourmaline}$ had the highest degradation rate. Figure 9b clearly shows that there is a kinetic linear relationship for the degradation of AR by each sample, which indicates that the degradation process of AR by all samples is highly consistent with the quasi-level kinetic equation. As shown in Table 1, the rate constant of $g\text{-C}_3\text{N}_4/\text{BiOI}/\text{tourmaline}$ is 0.0122 min^{-1} , which is significantly higher than the other samples and 1.56 times the degradation rate of pure $g\text{-C}_3\text{N}_4/\text{BiOI}$. This indicates that the addition of tourmaline contributes to the improvement in $g\text{-C}_3\text{N}_4$ photocatalytic performance. The reason for this may be that the addition of tourmaline greatly improved the absorbance of the samples, which is related to the effective separation of electron–hole pairs due to the strong electrostatic field of tourmaline, leading to an increase in photocatalytic activity [17].

Table 1. Photocatalytic degradation kinetic parameters of each sample.

Samples	$k \text{ (min}^{-1}\text{)}$	R^2
$g\text{-C}_3\text{N}_4$	0.0038	0.990
BiOI	0.0060	0.997
Tourmaline	0.0005	0.926
$g\text{-C}_3\text{N}_4/\text{BiOI}$	0.0078	0.992
$g\text{-C}_3\text{N}_4/\text{Tourmaline}$	0.0051	0.964
BiOI/Tourmaline	0.0069	0.996
$g\text{-C}_3\text{N}_4/\text{BiOI}/\text{Tourmaline}$	0.0122	0.993

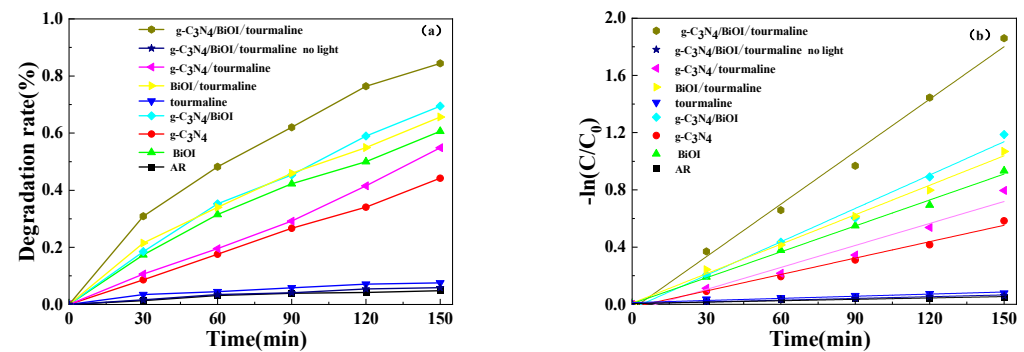


Figure 9. (a) Photocatalytic activity test of different materials; (b) kinetic linear fitting results of AR degradation of each sample.

3.3. Optimization of g-C₃N₄/BiOI/Tourmaline Composite Catalyst for the Degradation of AR Wastewater

3.3.1. Effect of Dosing Amount on the Degradation Rate of AR

Amaranth red wastewater with constant initial pH and an initial concentration of 10 mg/L was added with 0.5 g/L, 0.75 g/L, 1 g/L, 1.25 g/L, and 1.5 g/L of g-C₃N₄/BiOI/tourmaline, and degradation experiments were conducted under light to investigate the effect of g-C₃N₄/BiOI/tourmaline dosing on the photocatalytic performance of AR.

The amount of catalyst is one of the main parameters in degradation studies. In order to avoid using an excessive amount of catalyst, it is necessary to determine the optimal amount of addition for effective removal of dye molecules. The results in Figure 10a show that as the amount of catalyst increased from 0.5 g/L to 1 g/L, the degradation rate increased from 73.62% to 84.43% at 150 min of irradiation time. And the photodegradation efficiency decreased with the further increase in the amount of catalyst. As shown in Table 2, k increases and then decreases with the increase in the added amount. This may be attributed to the fact that, as the amount of photocatalyst increases, the number of active sites increases, which helps to enhance the absorption capacity of dye molecules and photon production. By contrast, when the amount of photocatalyst exceeds 1 g/L, the photocatalyst particles may cause light scattering and prevent light transmission in solution, and the particles may cause aggregation, which leads to a decrease in photodegradation efficiency [18]. From Figure 10b, it can be seen that $-\ln(C/C_0)$ for different g-C₃N₄/BiOI/tourmaline dosing amounts is linearly related to t , which is in accordance with the Langmuir–Hinshelwood quasi-level kinetic equation. Therefore, the optimal catalyst amount for effective degradation was 1 g/L.

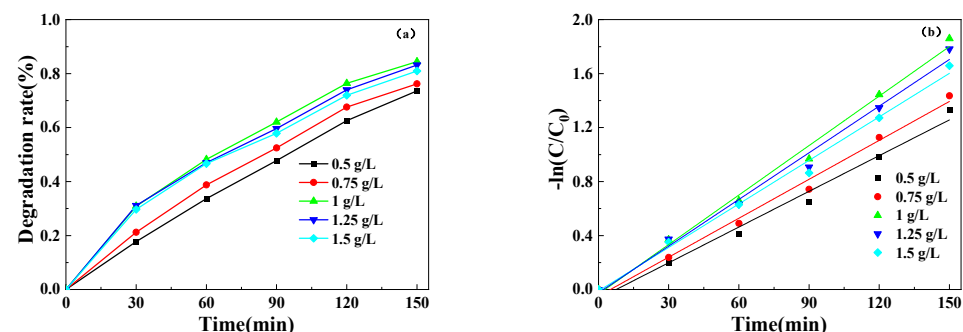


Figure 10. (a) Variation in degradation rate of solution with catalyst dosage; (b) effect of dosage on degradation kinetics.

Table 2. Effect of dosage on degradation kinetics.

Dosing Amount ($\text{g}\cdot\text{L}^{-1}$)	k (min^{-1})	R^2
0.5	0.0088	0.985
0.75	0.0096	0.992
1	0.0122	0.993
1.25	0.0115	0.990
1.5	0.0108	0.993

3.3.2. Effect of Initial pH on the Degradation Efficiency of AR

The process optimization was carried out by varying different pH levels for photodegradation experiments at an initial concentration of $10 \text{ mg}\cdot\text{L}^{-1}$ and a $\text{g-C}_3\text{N}_4/\text{BiOI}$ /tourmaline dosing of $1 \text{ g}\cdot\text{L}^{-1}$. The pH value of $10 \text{ mg}\cdot\text{L}^{-1}$ AR wastewater was adjusted with $1 \text{ mol}\cdot\text{L}^{-1}$ HCl or $1 \text{ mol}\cdot\text{L}^{-1}$ NaOH solution to make the initial pH values of amaranth red wastewater 1, 3, 5, 7, 9, 11, and 13.

The initial pH of the solution determines the nature of the surface charge, the size of the formed aggregates, the charge of the dye molecules, the adsorption of the dye on the surface, and the concentration of hydroxyl radicals, becoming an important parameter affecting the catalytic oxidation [19]. The effect of pH on AR photodegradation was studied in the pH range of 1–13. From Figure 11a and Table 3, it can be seen that for the dye removal, the degradation rate from pH 1 to 13 increases and then decreases, and the highest photocatalytic degradation rate was observed at pH 3 with a maximum degradation rate of 93.63% and a maximum k of 0.0169 min^{-1} . From Figure 11b, it can be seen that $-\ln(C/C_0)$ shows a linear relationship with t , which is in accordance with the quasi-first-order kinetic equation. This is because the acidic pH favors the generation of hydroxyl radicals, probably due to the positive charge of the catalyst solution in the acidic solution, which facilitates the movement of photogenerated electrons to the photocatalyst surface [20].

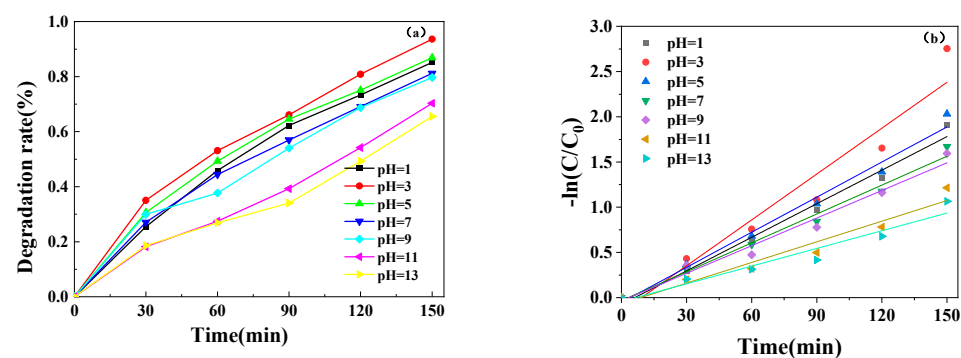


Figure 11. (a) Variation in degradation rate of solution with the pH value; (b) effect of AR initial pH on degradation kinetics.

Table 3. Effect of AR initial pH on degradation kinetics.

Initial pH	k (min^{-1})	R^2
1	0.0124	0.985
3	0.0169	0.936
5	0.0129	0.984
7	0.0107	0.986
9	0.0102	0.976
11	0.0076	0.949
13	0.0065	0.925

3.3.3. Effect of Initial Concentration on the Degradation Efficiency of AR

Under the conditions of a g-C₃N₄/BiOI/tourmaline addition of 1 g/L and a pH of 3, the initial concentrations of AR were varied from 5 to 10, 20, 30, 40, and 50 mg/L, and the effects of the initial concentrations of AR on the photocatalytic performance were investigated under light.

As shown in Figure 12a and Table 4, the decolorization efficiency decreased from 93.63% to 32.73% when the amaranth red concentration ranged from 10 to 50 mg/L. The decolorization rate and k-value of amaranth red decreased with the increase in the initial AR concentration, and the highest decolorization rate was achieved when the concentration was 10 mg/L. It can be seen from Figure 12b that there is a linear relationship between $-\ln(C/C_0)$ and t for different AR concentrations, and the reaction conforms to the Langmuir–Hinshelwood quasi-first-order kinetic equation. For all initial dye concentrations, the catalyst amount and light intensity are the same. Since the production of hydroxyl radicals is kept constant, the possibility of reaction of dye molecules with hydroxyl radicals is reduced. The path length of the photons entering the solution is also reduced at high initial dye concentrations. In addition, possible intermediates are formed, reducing the available surface active sites for the desired reaction and preventing degradation. Thus, the photocatalytic degradation efficiency is reduced, but the opposite effect is observed at low concentrations, which increases the absorption of photons by the catalyst [21].

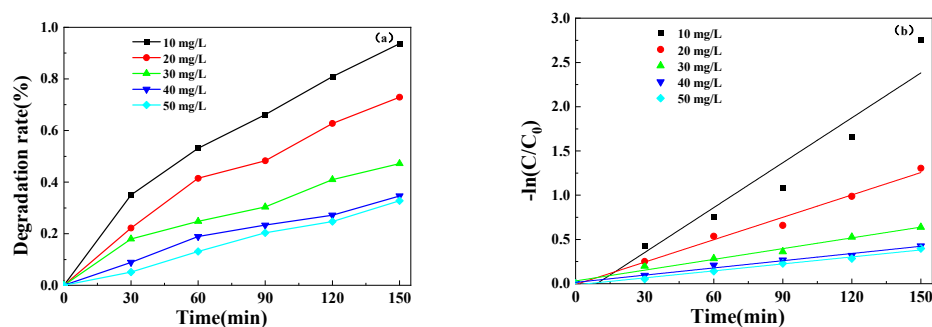


Figure 12. (a) Variation in degradation rate of solution with the initial concentration; (b) effect of initial concentration on degradation kinetics.

Table 4. Effect of initial concentration on degradation kinetics.

Initial Concentration (mg/L)	k (min ^{−1})	R^2
10	0.0169	0.934
20	0.0084	0.989
30	0.0041	0.983
40	0.0027	0.985
50	0.0026	0.991

A comparison of performance with other works investigating the photodegradation of amaranth dyes can be seen in Table 5.

Table 5. Comparison of performance with other studies on photodegradation of amaranth dyes.

Materials	Degradation Rate	References
g-C ₃ N ₄ /BiOI/tourmaline	93.63%	-
H ₂ O ₂ /TiO ₂	64%	[22]
TU (TiO ₂ using urea)	82.6%	[23]
FP1(polyvinyl alcohol–fomaldehyde binder films)	83.2%	[24]
Fe ⁰ /H ₂ O ₂	78%	[25]
Gd ₂ O ₃ /g-C ₃ N ₄	85%	[26]

As shown in Table 5, the photocatalytic degradation of amaranth red dye in our study has some advantages over other studies. Therefore, our study has some research significance in the photocatalytic degradation of amaranth red dye wastewater.

3.4. Reusable Performance of g-C₃N₄/BiOI/Tourmaline Photocatalysts

The stability of g-C₃N₄/BiOI/tourmaline as an important factor for practical applications was evaluated through five cyclic reactions of photodegradation of AR under light irradiation. As shown in Figure 13, this demonstrated the high stability of g-C₃N₄/BiOI/tourmaline. After five consecutive cycles under light irradiation, the catalyst exhibited an activity of 83.1%. These results indicate that the catalysts remain effective and reusable under light irradiation. The reduced effectiveness may be due to slight deactivation of the catalyst due to the adsorption of intermediate molecular fragments or the loss of catalyst mass during the cycling process [27].

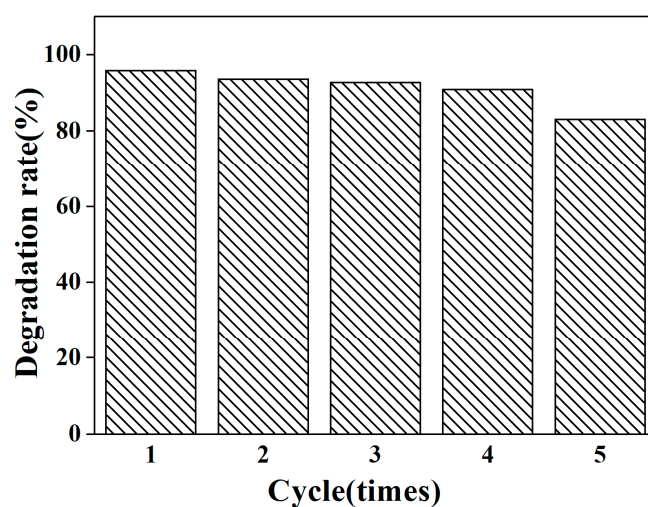


Figure 13. Effect of number of catalyst reuses on the photocatalytic performance.

3.5. Free Radical Masking Experiment

The removal of organic pollutants is attributed to the generation of various strong oxidizing substances (reactive groups such as h^+ , $-OH$, $SO_4^{\cdot-}$, and $-O_2^{\cdot-}$) in the photocatalytic reaction. To investigate the main reactive substances in this process, free radical scavenging experiments were performed. The results of the experiments are shown in Figure 14.

As shown in Figure 14, the degradation rate of AR solution was 93.63% in the composite reaction solution without any free radical scavenger. After adding the h^+ masking agent disodium EDTA to the reaction solution, the degradation rate of AR solution was 71.93%. The degradation rate of AR solution was 57.19% after the addition of $-OH$ masking agent isopropyl alcohol. After the addition of $-O_2^{\cdot-}$ masking agent p-benzoquinone to the reaction solution, the photocatalytic activity of the composites was significantly inhibited and the degradation rate of AR was only 19.28%. As shown in Figure 15, the masking rates of Na₂-EDTA, IPA, and BQ for the degradation experiments were 16%, 32.47%, and 69.94%, respectively. Thus, the results of the masking experiments indicate that $-O_2^{\cdot-}$ plays the most dominant role in the photocatalytic process, with $-OH$ playing the second most important role.

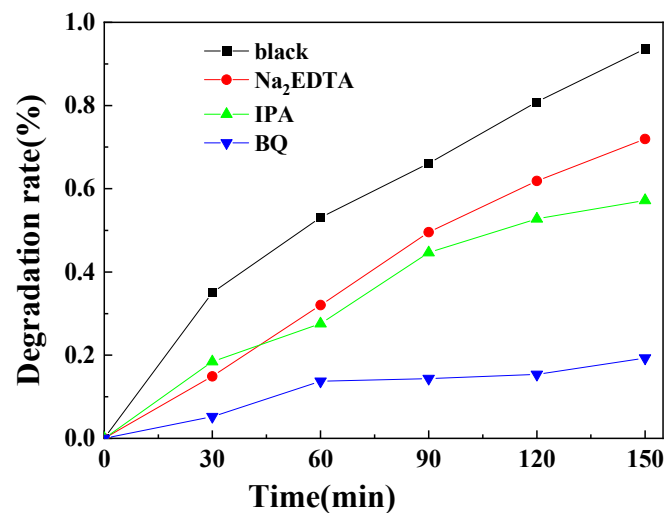


Figure 14. Effect of the scavengers on the degradation rate of solution.

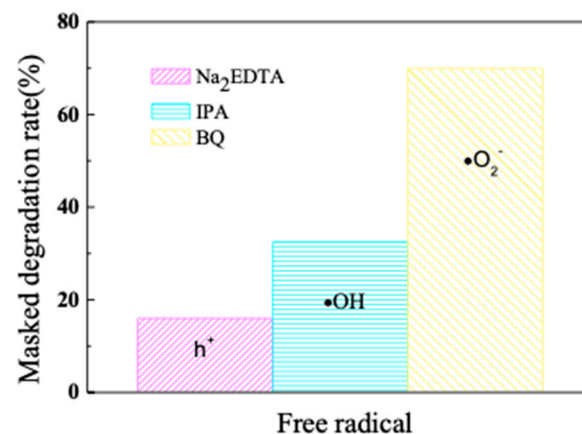


Figure 15. Free radical degradation masking rate.

The mechanistic diagram of the photoreaction is shown in Figure 16. To investigate the separation process of photogenerated electron–hole pairs, EVB and ECB were calculated using the following equations:

$$E_{VB} = \chi - E^e + 0.5 E_g \quad (2)$$

$$E_{CB} = E_{VB} - E_g \quad (3)$$

where χ is the geometric mean of the electronegativity of the semiconductor atoms, E_{VB} is the valence band energy, E_{CB} is the conduction band energy, E_g is the band gap energy of the semiconductor, and E^e (4.5 eV) is the energy of the free electron on the hydrogen atomic scale.

From the DRS analysis, the band gap energies of BiOI and g-C₃N₄ are 1.85 eV and 2.73 eV, respectively. The calculated EVBs of BiOI and g-C₃N₄ are estimated to be 2.62 eV and 1.61 eV based on Equations (2) and (3) above, and the resulting conduction band energies are 0.77 eV and −1.12 eV, respectively. Under light, both g-C₃N₄ and BiOI can be excited, but apparently, some photoexcited electrons in g-C₃N₄ will be transferred to the conduction band (CB) of BiOI since the CB energy of g-C₃N₄ is higher than that of BiOI. However, since the VB edge of BiOI is more positive than the VB edge of g-C₃N₄, the holes in the VB of BiOI will be transferred to the VB edge of g-C₃N₄. Since g-C₃N₄ is a reducing

photocatalyst and BiOI is an oxidizing photocatalyst, the photoinduced electron–hole pairs are effectively separated in the presence of forming heterojunctions [28].

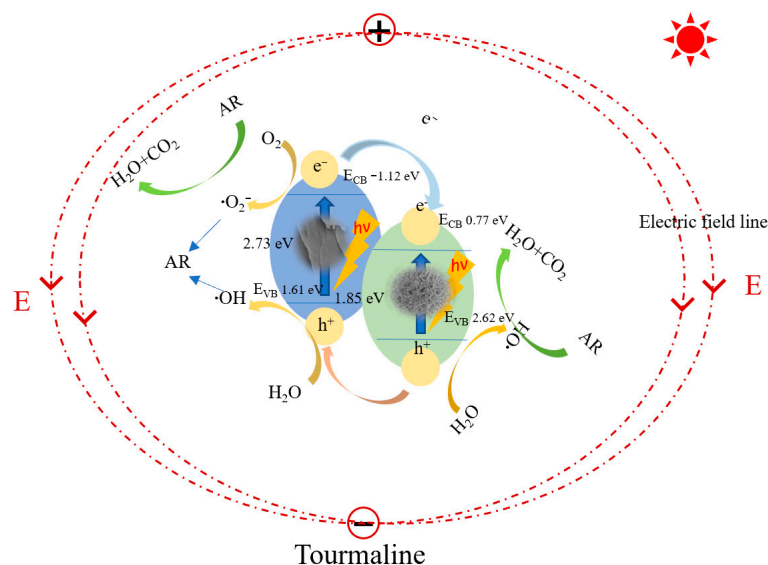


Figure 16. Photocatalytic mechanism diagram.

In addition, the electric field, far-infrared radiation, and polar coordination of tourmaline increase dissolved oxygen in water by ionizing water molecules and promote the degradation of AR [29]. The electric field of tourmaline drives the migration of photogenerated electrons and holes in g-C₃N₄ in opposite directions. The diffusion of electrons to the positively charged end of tourmaline and holes to the negatively charged end of tourmaline can promote the separation and transport of electrons and holes generated by g-C₃N₄ and BiOI, prolonging the lifetime of charge carriers and contributing to enhanced photodegradation activity [30]. And the electrons of g-C₃N₄ can react with adsorbed oxygen to generate $\cdot\text{O}_2^-$ radicals with strong oxidizing ability, because the conduction band potential energy of g-C₃N₄ is higher than that of $\text{O}_2/\cdot\text{O}_2^-$ (-0.33 eV) and the valence band potential energy of g-C₃N₄ ($+1.61$ eV) is lower than the reduction energy of $\text{OH}/\cdot\text{OH}$ ($+2.38$ eV) and $\text{H}_2\text{O}/\cdot\text{OH}$ ($+2.72$ eV). The EVB of BiOI is also higher than that of $\text{OH}/\cdot\text{OH}$ ($+2.38$ eV) active species [31]. This shows that $\cdot\text{O}_2^-$ is more oxidizing compared to other radicals, and, in agreement with the results of the radical experiments, can directly react with dye molecules to form the final product.

4. Summary

In summary, the g-C₃N₄/BiOI/tourmaline composite photocatalytic material was significantly enhanced compared with the single photocatalytic material, and single-factor experiments were conducted to optimize the g-C₃N₄/BiOI/tourmaline treatment of amaranth red-simulated wastewater and to perform kinetic analysis. The experimental results were obtained when the g-C₃N₄/BiOI/tourmaline dosage was 1 g/L and the initial pH of the solution was 3. The degradation rate of amaranth red solution could reach 93.63% with 150 min of light under the condition of an initial concentration of 10 mg/L. And its catalyst still exhibited an activity of 83.1% after 5 recycling and reuse cycles. The photocatalytic reaction mechanism of g-C₃N₄/BiOI/tourmaline was analyzed through free radical masking experiments. The results showed that the main active substances in the photocatalytic process of g-C₃N₄/BiOI/tourmaline were $\cdot\text{O}_2^-$.

Author Contributions: J.L. (Junsheng Li), J.L. (Jiahui Li) and Y.W. (writing—review and editing): preparation, creation, and/or presentation of the published work by those from the original research group, specifically, critical review, commentary, or revision—including pre- or post-publication stages. M.X. (formal analysis): application of statistical, mathematical, computational, or other formal

techniques to analyze or synthesize study data. Z.X. and J.Z. (conceptualization): ideas; formulation, or evolution of overarching research goals and aims. L.J. and C.T. (resources): provision of study materials, reagents, materials, patients, laboratory samples, animals, instrumentation, computing resources, or other analysis tools. All authors have read and agreed to the published version of the manuscript.

Funding: 2023 Heilongjiang Natural Science Foundation Joint Guidance Project (LH2023E029).

Institutional Review Board Statement: Not applicable.

Informed Consent Statement: Not applicable.

Data Availability Statement: The data presented in this study are available in this article.

Conflicts of Interest: The authors declare no conflict of interest.

References

1. Aramesh, N.; Bagheri, A.R.; Bilal, M. Chitosan-based hybrid materials for adsorptive removal of dyes and underlying interaction mechanisms. *Int. J. Biol. Macromol.* **2021**, *183*, 399–422. [\[CrossRef\]](#)
2. Januário, E.F.D.; Vidovich, T.B.; Beluci, N.D.C.L.; Paixão, R.M.; da Silva, L.H.B.R.; Homem, N.C.; Bergamasco, R.; Vieira, A.M.S. Advanced graphene oxide-based membranes as a potential alternative for dyes removal: A review. *Sci. Total Environ.* **2021**, *789*, 147957. [\[CrossRef\]](#) [\[PubMed\]](#)
3. Banerjee, S.; Debnath, A.; Allam, B.K.; Musa, N. Adsorptive and photocatalytic performance of perovskite material for the removal of food dye in an aqueous solution. *Environ. Chall* **2021**, *5*, 100240. [\[CrossRef\]](#)
4. Gonçalves, J.; da Silva, K.; Rios, E.; Crispim, M.; Dotto, G. Chitosan hydrogel scaffold modified with carbon nanotubes and its application for food dyes removal in single and binary aqueous systems. *Biol. Macromol.* **2020**, *142*, 85–93. [\[CrossRef\]](#) [\[PubMed\]](#)
5. Jindal, H.; Kumar, D.; Sillanpää, M. Current progress in polymeric graphitic carbon nitride-based photocatalysts for dye degradation. *Inorg. Chem. Commun.* **2021**, *131*, 108786. [\[CrossRef\]](#)
6. Ye, L.; Su, Y.; Jin, X.; Xie, H.; Zhang, C. Recent advances in BiOX (X = Cl, Br and I) photocatalysts: Synthesis, modification, facet effects and mechanisms. *Environ. Sci. Nano* **2014**, *1*, 90. [\[CrossRef\]](#)
7. Sun, H.J.; Liu, X.G.; Chen, Z.H.; Chen, L.X.; Deng, Y.R.; Mei, Y.Y. Study on photocatalytic degradation of methyl orange by BiOI/g-C₃N₄. *Inorg. Salt Ind.* **2021**, *53*, 90–94.
8. Yuan, J. Preparation of Tourmaline Based Composites and Their Application to Dye and Ammonia Nitrogen Wastewater. Master's Thesis, Tianjin University of Technology, Tianjing, China, 2021.
9. He, D.; Zhang, L.; Shu, X.; Liu, S. Preparation of nano-ZnO/tourmaline composite powder and its photocatalytic performance on methylene blue. *New Chem. Mater.* **2018**, *46*, 93–96.
10. Huang, J.H.; Lin, W.T.; Xie, L.Y.; Chen, J.Q. Construction of graphite-phase carbon-carbon nitride-bismuth iodide layered heterojunction and its photocatalytic bactericidal performance. *Environ. Sci.* **2017**, *38*, 3979–3986.
11. Tian, N.; Huang, H.; Wang, S.; Zhang, T.; Du, X.; Zhang, Y. Facet-charge-induced coupling dependent interfacial photocharge separation: A case of BiOI/g-C₃N₄ p-n junction. *Appl. Catal. B Environ.* **2020**, *267*, 118697. [\[CrossRef\]](#)
12. Shi, L.; Liang, L.; Ma, J.; Meng, Y.; Zhong, S.; Wang, F.; Sun, J. Highly efficient visible light-driven Ag/AgBr/ZnO composite photocatalyst for degrading Rhodamine B. *Ceram. Int.* **2014**, *40*, 3495–3502. [\[CrossRef\]](#)
13. Nie, W.; Chen, T.; Chen, Z.; Wu, S.; Cao, N. Study of high porosity tourmaline ceramics for the treatment of coking wastewater. *Coal Chem. Ind.* **2016**, *44*, 44–46.
14. Liu, H.; Zhou, H.; Liu, X.; Li, H.; Ren, C.; Li, X.; Li, W.; Lian, Z.; Zhang, M. Engineering design of hierarchical g-C₃N₄@Bi/BiOBr ternary heterojunction with Z-scheme system for efficient visible-light photocatalytic performance. *J. Alloys Compd.* **2019**, *798*, 741–749. [\[CrossRef\]](#)
15. Fan, Y. Effect of terbium to tourmaline ratio on the morphology and optical properties of Tb/tourmaline/TiO₂ nanotubes. *Contemp. Chem. Ind.* **2017**, *46*, 1560–1563+1567.
16. Wei, L.; Wang, X.; Liu, S.; Guo, W. Preparation of tourmaline sphere-loaded nanotitanium dioxide photocatalysts and their degradation of phthalate esters in water. *Sichuan Environ.* **2018**, *37*, 35–38.
17. Qi, S.; Wang, D.; Zhao, Y.; Xu, H. Photocatalytic mechanism of tourmaline/ZnO composites. *Mater. Eng.* **2019**, *47*, 145–151.
18. Jiang, R.; Zhu, H.Y.; Li, J.B.; Fu, F.Q.; Yao, J.; Jiang, S.T.; Zeng, G.M. Fabrication of novel magnetically separable BiOBr/CoFe₂O₄ microspheres and its application in the efficient removal of dye from aqueous phase by an environment-friendly and economical approach. *Appl. Surf. Sci.* **2016**, *364*, 604–612. [\[CrossRef\]](#)
19. Hu, L.; Chen, F.; Hu, P.; Zou, L.; Hu, X. Hydrothermal Synthesis of SnO₂/ZnS Nanocomposite as a Photocatalyst for Degradation of Rhodamine B under Simulated and Natural Sunlight. *J. Mol. Catal. A Chem.* **2016**, *411*, 203–213. [\[CrossRef\]](#)
20. Rajamanickam, D.; Dhatshanamurthi, P.; Shanthi, M. Enhanced photocatalytic efficiency of NiS/TiO₂ composite catalysts using sunset yellow, an azo dye under day light illumination. *Mater. Res. Bull.* **2015**, *61*, 439–447. [\[CrossRef\]](#)

21. Foroughirad, S.; Haddadi-Asl, V.; Khosravi, A.; Salami-Kalajahi, M. Synthesis of magnetic nanoparticles-decorated halloysite nanotubes/poly([2-(acryloyloxy) ethyl] trimethylammonium chloride) hybrid nanoparticles for removal of Sunset Yellow from water. *J. Polym. Res.* **2020**, *27*, 320.
22. Gupta, V.K.; Jain, R.; Mittal, A.; Saleh, T.A.; Nayak, A.; Agarwal, S.; Sikarwar, S. Photo-catalytic degradation of toxic dye amaranth on TiO₂/UV in aqueous suspensions. *Mater. Sci. Eng. C* **2012**, *32*, 12–17. [[CrossRef](#)] [[PubMed](#)]
23. Naik, A.P.; Salkar, A.V.; Majik, M.S.; Morajkar, P.P. Enhanced photocatalytic degradation of Amaranth dye on mesoporous anatase TiO₂: Evidence of C–N, N=N bond cleavage and identification of new intermediates. *Photochem. Photobiol. Sci.* **2017**, *16*, 1126–1138. [[CrossRef](#)] [[PubMed](#)]
24. Kumar, J.; Bansal, A. Photodegradation of amaranth in aqueous solution catalyzed by immobilized nanoparticles of titanium dioxide. *Int. J. Environ. Sci. Technol.* **2012**, *9*, 479–484. [[CrossRef](#)]
25. Devi, L.G.; Rajashekhar, K.E.; Raju, K.A.; Kumar, S.G. Influence of various aromatic derivatives on the advanced photo Fenton degradation of Amaranth dye. *Desalination* **2011**, *270*, 31–39. [[CrossRef](#)]
26. Aditya, M.; Chellapandi, T.; Prasad, G.K.; Venkatesh, M.J.P.; Khan, M.R.; Madhumitha, G.; Roopan, S.M. Biosynthesis of rod shaped Gd₂O₃ on g-C₃N₄ as nanocomposite for visible light mediated photocatalytic degradation of pollutants and RSM optimization. *Diam. Relat. Mater.* **2022**, *121*, 108790. [[CrossRef](#)]
27. Luo, J.; Zhou, X.; Ma, L.; Xu, X. Enhanced Visible-Light-Driven Photocatalytic Activity of WO₃/BiOI Heterojunction Photocatalysts. *J. Mol. Catal. A Chem.* **2015**, *410*, 168–176. [[CrossRef](#)]
28. He, R.; Cheng, K.; Wei, Z.; Zhang, S.; Xu, D. Room-temperature in situ fabrication and enhanced photocatalytic activity of direct Z-scheme BiOI/g-C₃N₄ photocatalyst. *Appl. Surf. Sci.* **2018**, *465*, 964–972. [[CrossRef](#)]
29. Zhu, A.; Chen, F.; Liu, S.; Bu, X. Study on the adsorption performance of ultra-fine tourmaline powder on methylene blue in water. *J. Wuhan Light Ind. Univ.* **2017**, *36*, 48–52+56.
30. Yu, L.; Wang, C.; Chen, F.; Zhang, J.; Ruan, Y.; Xu, J. Investigating the synergistic effects in tourmaline/TiO₂-based heterogeneous photocatalysis: Underlying mechanism insights. *J. Mol. Catal. A Chem.* **2016**, *411*, 1–8. [[CrossRef](#)]
31. Wan, S.; Ou, M.; Zhong, Q.; Zhang, S. Z-scheme CaIn₂S₄/Ag₃PO₄ nanocomposite with superior photocatalytic NO removal performance: Fabrication, characterization and mechanistic study. *New J. Chem.* **2018**, *42*, 318–326. [[CrossRef](#)]

Disclaimer/Publisher's Note: The statements, opinions and data contained in all publications are solely those of the individual author(s) and contributor(s) and not of MDPI and/or the editor(s). MDPI and/or the editor(s) disclaim responsibility for any injury to people or property resulting from any ideas, methods, instructions or products referred to in the content.